Monthly Notices
of the
ROYAL ASTRONOMICAL SOCIETY

MNRAS **458,** 1803–1814 (2016)
Advance Access publication 2016 February 23

doi:10.1093/mnras/stw419

A newly discovered radio halo in merging cluster MACS J2243.3-0935

T. M. Cantwell,[1]★ A. M. M. Scaife,[1] N. Oozeer,[2,3,4] Z. L. Wen[5] and J. L. Han[5]

[1]*Jodrell Bank Centre for Astrophysics, Alan Turing Building, Oxford Road, Manchester M13 9PL, UK*
[2]*SKA South Africa, The Park, Park Road, Pinelands, Cape Town 7405, South Africa*
[3]*African Institute for Mathematical Sciences, 6-8 Melrose Road, Muizenberg 7945, South Africa*
[4]*Centre for Space Research, North-West University, Potchefstroom 2520, South Africa*
[5]*National Astronomical Observatories, Chinese Academy of Sciences, 20A Datun Road, Chaoyang District, Beijing 100012, China*

Accepted 2016 February 19. Received 2016 February 18; in original form 2015 November 18

ABSTRACT

We report the discovery of a radio halo in the massive merging cluster MACSJ2243.3-0935, as well as a new radio relic candidate, using the Giant Meterwave Radio Telescope and the Karoo Array Telescope-7 telescope. The radio halo is coincident with the cluster X-ray emission and has a largest linear scale of approximately 0.9 Mpc. We measure a flux density of 10.0 ± 2.0 mJy at 610 MHz for the radio halo. We discuss equipartition estimates of the cluster magnetic field and constrain the value to be of the order of 1 μG. The relic candidate is detected at the cluster virial radius where a filament meets the cluster. The relic candidate has a flux density of 5.2 ± 0.8 mJy at 610 MHz. We discuss possible origins of the relic candidate emission and conclude that the candidate is consistent with an infall relic.

Key words: galaxies: clusters: intracluster medium.

1 INTRODUCTION

Galaxy clusters are the largest viralized structures in the Universe with typical masses of order 10^{15} $M_{\odot}$. Most of this mass is composed of dark matter. The other 10–20 per cent is contained in baryonic matter, with the mass in the hot intra-cluster medium (ICM) being about 10 times larger than the mass contained in galaxies (Kravtsov & Borgani 2012; Brunetti & Jones 2014). The ICM was first detected in the X-ray band, emitting via thermal bremsstrahlung, indicating that the ICM is a thermalized plasma (Voit 2005). However the detection of Mpc-scale diffuse emission in the radio band provides evidence that cosmic ray electrons (CRe) are also present in the ICM, as are cluster-scale magnetic fields (Feretti et al. 2012; Brunetti & Jones 2014). As such, radio observations of clusters provide a unique opportunity to study the non-thermal populations of the ICM.

The dynamics and evolution of galaxy clusters can also be indirectly probed using radio observations. Diffuse radio emission in clusters is divided into three morphological classes: radio relics; giant radio haloes; mini haloes. Radio relics are normally elongated structures found at the periphery of clusters and can be highly polarized. Giant radio haloes are usually found at the centre of clusters and typically have a more rounded morphology than radio relics. Giant radio haloes tend to be largely unpolarized due to a high degree of either beam or internal depolarization. Both giant radio haloes and radio relics have typical physical sizes of 1 Mpc. Both radio haloes and radio relics are thought to be linked to cluster mergers where shocks and turbulence are expected to accelerate electrons to relativistic energies. See Feretti et al. (2012) and references therein for a review on diffuse radio emission in clusters.

Since their discovery, a number of empirical scaling relations have been found between the radio power of giant radio haloes and the properties of the host cluster such as cluster mass, temperature and X-ray luminosity (Colafrancesco 1999; Govoni et al. 2001; Enßlin & Röttgering 2002; Feretti 2002, 2003; Brunetti et al. 2009; Cassano et al. 2013; Yuan, Han & Wen 2015). The most well-studied scaling relationship is between the radio power at 1.4 GHz, $P_{1.4}$, and the X-ray luminosity, $L_{\rm x}$, of the ICM. When both clusters with a radio halo and radio quiet clusters are examined, a bimodality is found in the distribution on the radio–X-ray plane, with radio loud clusters exhibiting a correlation and radio quiet clusters showing none (Cassano et al. 2013). This bimodality is also found to correspond to the dynamical state of the cluster, further linking radio haloes to cluster mergers.

More recently a correlation between the radio power of haloes at 1.4 GHz and the integrated Sunyaev–Zel'dovich (SZ) effect measurements, Y_{500} was reported by Basu (2012). No bimodality in the cluster distribution was seen in the sample reported by Basu (2012); however, a more statistically complete study by Cassano et al. (2013) reported a bimodal distribution of clusters in the $P_{1.4}$–Y_{500} diagrams.

MACS J2243.3-0935 is a massive galaxy cluster at a redshift of $z = 0.447$ at the centre of the supercluster SCL2243-0935 (Schirmer et al. 2011). Table 1 lists some important properties of MACS J2243.3-0935 determined from previous studies across a range of wavelengths (Ebeling et al. 2010; Mantz et al. 2010; Mann & Ebeling 2012; Planck Collaboration XXIX 2014; Wen & Han 2013).

★E-mail: therese.cantwell@postgrad.manchester.ac.uk

Table 1. Properties of MACS J2243.3-0935.

Property	Value	Reference
z	0.447	Ebeling et al. (2010)
M_{500} ($\times 10^{14}$M$_\odot$)	10.07 ± 0.58	Planck Collaboration XXIX (2014)
Y_{500} (Mpc^2)	16.3 ± 1.7	Planck Collaboration XXIX (2014)
$L_{x,\,500}$ (10^{44}erg s^{-1})	11.56 ± 0.67	Mantz et al. (2010)
T (keV)	8.24 ± 0.92	Mantz et al. (2010)
w (kpc)	156±4	Mann & Ebeling (2012)
Γ	-1.53 ± 0.07	Wen & Han (2013)
Virial radius (Mpc)	$2.13^{+0.18}_{-0.12}$	Schirmer et al. (2011)

L_x is core excised from 0.1–2.4 kev.

Table 2. Observation details of MACS J2243.3-0935.

Telescope	GMRT	KAT-7
Date	2014 June 20	2012 September 7
Frequency (MHz)	610	1826
Time on target (h)	5.6	7.5
Usable time (h)	5.6	7.5
Bandwidth (MHz)	33	400
Usable bandwidth (MHz)	29	256
No. channels	256	600
No. averaged channels	28	9
per cent flagged	33 per cent	18.5 per cent
Sensitivity	40 μJy	500 μJy
Angular resolution	∼5 arcsec	∼3 arcmin
FOV	43 arcmin	∼60 arcmin

The dynamical state of this cluster has been examined using a variety of techniques. Mann & Ebeling (2012) use the X-ray morphology and the offset between the brightest cluster galaxy (BCG) and X-ray peak/centroid to characterize the dynamical state of clusters. They find that the merger axis suggested by the highly elongated X-ray emission in MACS J2243.3-0935 is mis-aligned with the merger axis suggested by the two main galaxy concentrations. Mann & Ebeling (2012) also report a separation between the BCG and the X-ray peak of 125 ± 6 kpc and a centroid shift, w, of 156 ± 4 kpc.

Wen & Han (2013) calculate the relaxation parameter, Γ, of MACS J2243.3-0935 to be -1.53 ± 0.07. The relaxation parameter measures the amount of substructure in a galaxy cluster based on the cluster's optical properties. Positive values of Γ indicate a relaxed system and negative values of Γ indicate a disturbed cluster. The relaxation parameter separates relaxed and unrelaxed clusters with a success rate of 94 per cent. Wen & Han (2013) find a correlation between the relaxation parameter and the offset of the halo radio power from that expected from the $P_{1.4\,\mathrm{GHz}}$–L_x relation. This provides further evidence that the dynamical state of the cluster plays an important role in the generation of a radio halo and that the relaxation parameter could prove a powerful tool for identifying possible host clusters of diffuse radio emission. The highly negative relaxation parameter of MACS J2243.3-0935, as well as its high luminosity, were the primary reasons for selecting this cluster for study in this work.

MACS J2243.3-0935 has also been detected by *Planck* as PSZ2 G056.93-55.08 (Planck Collaboration XXVII 2015). From these data, the total mass measured from the SZ effect for this cluster is 1.007×10^{15} M$_\odot$ and the cluster has an integrated Compton-y parameter, $Y = 16.3 \pm 1.7$ arcsec^2. In the radio, the cluster field was observed by the NRAO VLA Sky Survey (NVSS; Condon et al. 1998) and the Faint Images of the Radio Sky at Twenty-cm survey (FIRST; Becker, White & Helfand 1995) however the field is not covered by the Sydney University Molonglo Sky Survey (Bock, Large & Sadler 1999) or the Westerbork Northern Sky Survey (Rengelink et al. 1997).

In this paper, we present new observations of MACS J2243.3-0935 at 1.4 GHz using the Karoo Array Telescope[1] (KAT-7) and at 610 MHz with the Giant Metre Wave Telescope (GMRT) (Swarup et al. 1991). In Section 2, we describe the observations and data reduction. In Section 3, we present our results which are then discussed in Section 4 before making our concluding remarks in Section 5.

In this work, a Λcold dark matter cosmology is assumed with $H_0 = 70\,\mathrm{km\,s^{-1}\,Mpc^{-1}}$, $\Omega_m = 0.3$, $\Omega_\Lambda = 0.7$. Using these parameters, at a redshift of 0.447, 1 arcsec corresponds to a physical scale of 5.74 kpc (Wright 2006).

2 OBSERVATIONS AND DATA REDUCTION

MACS J2243.3-0935 was observed at 1.8 GHz by KAT-7 and at 610 MHz with the GMRT.

The GMRT is an array of 30 antennas with diameters of 45 m in India. 14 antenna make up the central core of the array while the remaining 16 antennas are arranged around the core to form a Y-shape. This distribution of antennas affords good uv coverage on both the short and long baselines. The GMRT is capable of observing at a range of frequencies from 150 to 1280 MHz with a maximum bandwidth of 33 MHz. At 610 MHz the maximum resolution is about 5 arcsec and the half power point of the primary beam is 43 arcmin.

KAT-7 is an array of seven antennas with diameters of 12 m in South Africa. KAT-7 can observe at central frequencies of 1382 and 1826 MHz with a bandwidth of 256 MHz. The maximum resolution of KAT-7 is 4 arcmin at 1382 MHz and 3 arcmin at 1826 MHz.

A summary of the observational details can be found in Table 2.

2.1 KAT-7

KAT-7 was used to observe MACS J2243.3-0935 on the 2012-09-08. All seven antennas were used for this observation at a frequency of 1822 MHz with a bandwidth of 400 MHz. Due to analogue filters in the IF and baseband system, only the central 256 MHz of the bandwidth is useable. A first round of flagging was carried by the automatic flagging routine (developed in-house) to remove known radio frequency interference (RFI). The data were furthermore flagged inside CASA to remove other low-level RFI. PKS 1934-638 was used as the primary calibrator and PKS2243-123 as the phase calibrator. The flux calibrator was observed every 2 h for 2 min while the phase calibrator was observed every 15 min for 3 min. Flux densities were tied to the Perley–Butler 2010 flux density scale (Perley & Butler 2013). Standard data flagging and calibration was carried out in CASA4.3. Three rounds of phase only selfcal were performed. The data were then imaged using the multifrequency, multiscale clean task in CASA with a briggs weighting robust parameter of 0. The resulting image has an rms of 0.5 mJy. Fig. 1 shows the full field KAT-7 image of MACS J2243.3-0935 while Fig. 2 shows the central cluster region.

[1] For more information, see http://public.ska.ac.za/kat-7

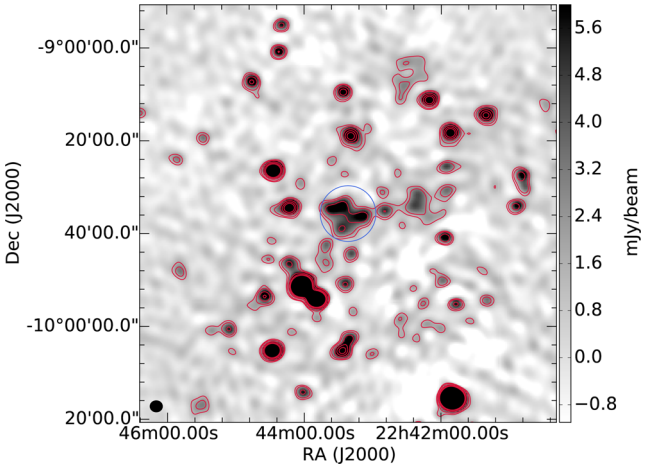

Figure 1. Grey-scale plot showing the KAT-7 FOV image of MACS J2243.3-0935 with KAT-7 contours overlaid in red. Contours are at 3, 5, 10, 15, 20 × $\sigma_{\rm rms}$ where $\sigma_{\rm rms} = 500\,\mu{\rm Jy\,beam^{-1}}$. The resolution is 160.10×144.99 arcsec. The blue circle marks the viral radius of MACS J2243.3-0935. The virial radius is $2.13^{+0.18}_{-0.12}$ Mpc or 370 arcsec.

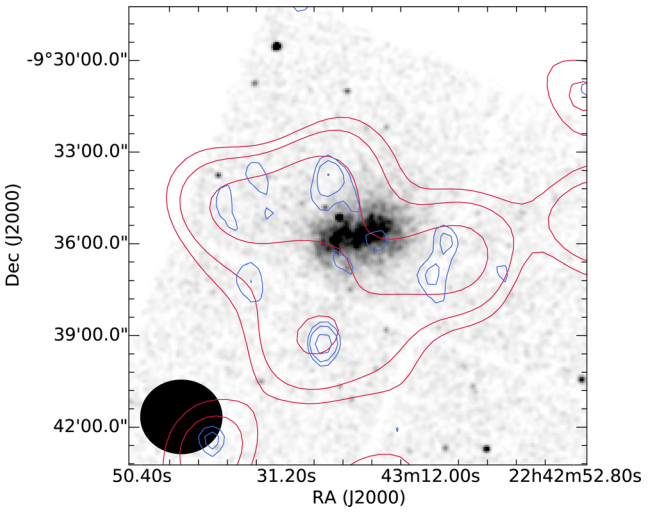

Figure 2. Grey-scale plot showing X-ray image of MACS J2243.3-0935 in the *Chandra* ACIS 0.5–7 keV band. The image has been smoothed with a Gaussian kernel with $\sigma = 3$ pixels. KAT-7 contours are overlaid in red while NVSS contours are overlaid in blue. Contours are at 3, 5, 10, 15, 20 × $\sigma_{\rm rms}$ where $\sigma_{\rm rms} = 500\,\mu{\rm Jy\,beam^{-1}}$ for KAT-7 and $\sigma_{\rm rms} = 400\,\mu{\rm Jy\,beam^{-1}}$ for NVSS. The resolution of the KAT-7 image is 160.10×144.99 arcsec while the resolution of the NVSS image is 45 arcsec × 45 arcsec

2.2 GMRT

MACS J2243.3-0935 was observed by the GMRT at 610 MHz with a bandwidth of 33 MHz on 2014 June 20.[2] The primary calibrator, 3C48, was observed for 15 min at the start of the observations and 3C468.1 was observed at the end of the observation in order

[2] MACS J2243.3-0935 was also observed by the GMRT for 7 h on 2010 October 25 at 610 and 235 MHz. These observations were taken before upgrades began on the GMRT and are of lower quality than the new observations and are significantly contaminated with RFI. Including these data does not improve the image quality.

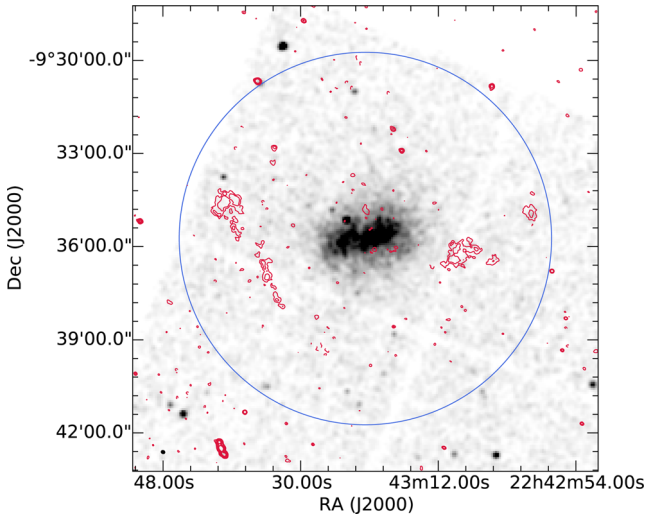

Figure 3. Grey-scale plot showing X-ray image of MACS J2243.3-0935 in the *Chandra* ACIS 0.5–7 keV band. The image has been smoothed with a Gaussian kernel with $\sigma = 3$ pixels. The red contours show the naturally weighted GMRT image. Contours are at −3, 3, 5, 10, 15, 20 × $\sigma_{\rm rms}$ where $\sigma_{\rm rms} = 45\,\mu{\rm Jy\,beam^{-1}}$. The resolution of the GMRT image is 7.44 arcsec×6.06 arcsec. Radio point sources have been subtracted from this image. The blue circle marks the viral radius of MACS J2243.3-0935. The virial radius is $2.13^{+0.18}_{-0.12}$ Mpc or 370 arcsec.

to test the flux calibration. The phase calibrator J2225-049 was observed for 5 min, every 20 min. Data reduction and calibration for GMRT data at 610 MHz were carried out in CASA (McMullin et al. 2007). The calibration process followed that described in De Gasperin et al. (2014). Calibration and flagging were performed in an iterative fashion. Data were phase-, amplitude- and bandpass-calibrated, then flagged, in the first round, using first the rflag mode in the CASA task flagdata and, in the second round, with AOFLAGGER (Offringa, van de Gronde & Roerdink 2012). After flagging with AOFLAGGER, the data were averaged and a final round of calibration and flagging with AOFLAGGER was performed. Five rounds of phase only selfcal were carried out. After calibration and selfcal, approximately 33 per cent of the data were flagged. Flux densities were tied to the Perley–Butler 2010 flux density scale (Perley & Butler 2013). The flux density measured from 3C468.1 was 12.5 ± 0.9 Jy, which agrees within error with the literature value of 12.7 Jy (Pauliny-Toth, Wade & Heeschen 1966; Helmboldt et al. 2008). The data were then imaged using the multifrequency, multiscale clean task in CASA.

To subtract the point source population, data from baselines longer than 4 kλ, which corresponds to an angular scale of 50 arcsec, were imaged with a Briggs robust parameter of 0. The resulting image had an rms of 40 μJy beam^{-1} and a resolution of 4.84 arcsec × 4.15 arcsec. The clean components for compact sources in the cluster were then Fourier transformed and subtracted from the *uv* data using the CASA tasks ft and uvsub. Two images were then made using the point source subtracted data: the first was naturally weighted with no uvtaper and the second was naturally weighted with a uvtaper of 5 kλ by 4 kλ. The naturally weighted image has a resolution of 7.44 arcsec × 6.06 arcsec and an rms of 45 μJy beam^{-1} and is shown in Fig. 3. The tapered image with a resolution of 44.89 arcsec × 33.70 arcsec and an rms of 200 μJy beam^{-1} and is shown in Fig. 4.

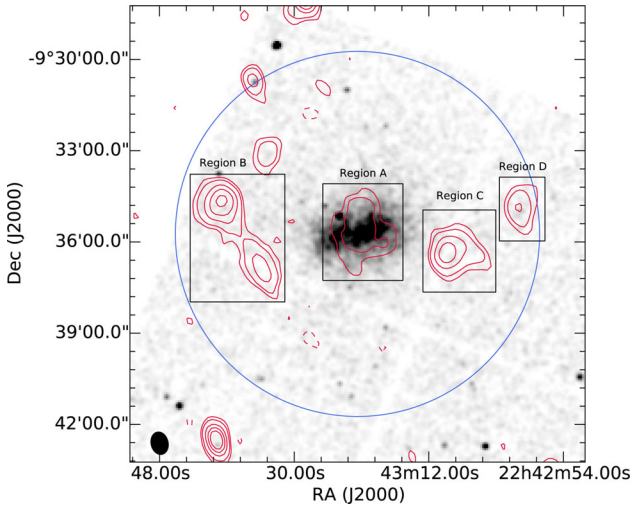

Figure 4. Grey-scale plot showing X-ray image of MACS J2243.3-0935 in the Chandra ACIS 0.5–7 keV band. The image has been smoothed with a Gaussian kernel with $\sigma = 3$ pixels. The red contours show the naturally weighted GMRT image with a uvtaper of 5×4 kλ. Contours are at −3, 3, 5, 10, 15, 20 × $\sigma_{\rm rms}$ where $\sigma_{\rm rms} = 200$ μJy beam^{-1}. The resolution of the GMRT image is 44.89 arcsec × 33.70 arcsec. Radio point sources have been subtracted from this image. The blue circle marks the viral radius of MACS J2243.3-0935. The virial radius is $2.13^{+0.18}_{-0.12}$ Mpc or 370 arcsec. Different regions of diffuse radio emission are marked with black rectangles and labelled.

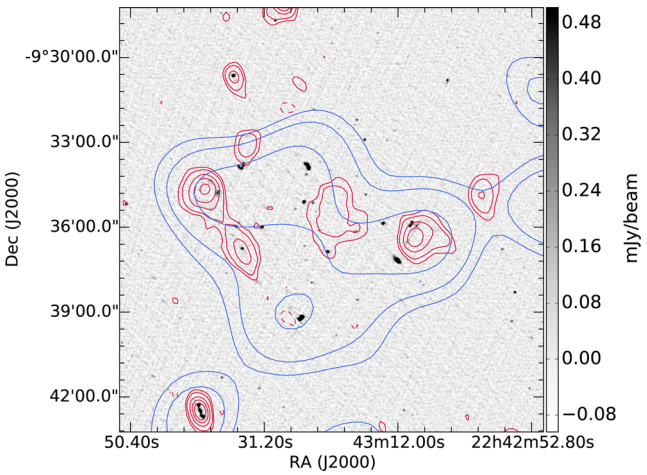

Figure 5. Grey-scale image shows the robust 0 high-resolution GMRT data used for the point source subtraction. KAT-7 contours are overlaid in blue while contours for the tapered, point source subtracted GMRT image are overlaid in red. Contours are at 3, 5, 10, 15, 20 × $\sigma_{\rm rms}$ where $\sigma_{\rm rms} = 500$ μJy beam^{-1} for KAT-7 and −3, 3, 5, 10, 15, 20 × $\sigma_{\rm rms}$ $\sigma_{\rm rms} = 200$ μJy beam^{-1} for the GMRT. The resolution of the KAT-7 image is 160.10×144.99 arcsec. The resolution of the high-resolution GMRT image is 7.44 arcsec × 6.06 arcsec while the resolution of the tapered GMRT image is 44.89 arcsec × 33.70 arcsec.

3 RESULTS

3.1 MACS J2243.3-0935 at >1 GHz

Fig. 1 shows the KAT-7 image of MACS J2243.3-0935 at 1822 MHz. The resolution of the image is 160.10 arcsec × 144.99 arcsec. However, the fidelity of the KAT-7 image is limited by the presence of a bright complex source to the south west of the field of view (FOV). A large region of diffuse emission can be seen towards the cluster centre with a largest linear scale (LLS) of 3.9 Mpc. This diffuse emission is detected at a 5σ level. The flux density of the cluster emission detected by KAT-7, measured within the 3σ level, is 40 ± 6 mJy. Comparison with NVSS in Fig. 2 shows that there are at least two unresolved point sources in this region. Given the low resolution of these data, it is not possible to characterize the emission in the KAT-7 image furthermore than to note that diffuse emission appears to be present in addition to these compact sources.

3.2 MACS J2243.3-0935 at <1 GHZ

Figs 3 and 4 show diffuse radio emission detected in MACS J2243.3-0935 by the GMRT at 610 MHz. In the GMRT images, the diffuse emission detected by KAT-7 is resolved into four distinct regions labelled A–D in Fig. 4. Table 3 lists the flux densities for each of these regions. Flux densities were measured from the naturally weighted uvtapered image from within the 3σ contour level. Errors in flux measurements were calculated using the formula:

$$\sigma_{S_{610}} = \sqrt{(\sigma_{\rm cal} S_{610})^2 + \left(\sigma_{\rm rms}\sqrt{N_{\rm beam}}\right)^2}, \quad (1)$$

where $\sigma_{\rm cal}$ is the uncertainty in the calibration of the flux scale and $N_{\rm beam}$ is the number of independent beams in the source. $\sigma_{\rm cal}$ is taken to be 10 per cent for the GMRT (Chandra, Ray & Bhatnagar 2004). Fig. 5 shows the high-resolution GMRT image of MACS J2243.3-0935 used to subtract the point sources with contours of the GMRT tapered image and KAT-7 image overlaid. The flux measured from the high-resolution GMRT image within the same region of the KAT-7 cluster emission at a 3σ level is approximately 63 mJy. Extrapolating this flux to 1826 MHz assuming a spectral index of $\alpha = 0.7$, where $S_\nu \propto \nu^{-\alpha}$, gives a value of approximately 29 mJy. Subtracting this from the KAT-7 flux calculated in Section 3.1 leaves a residual flux of 11 mJy. The total flux measured from the point source subtracted, tapered GMRT image within the same region of the KAT-7 cluster emission is approximately 40 mJy. This suggests that the average spectral index of the diffuse emission in MACS J2243.3-0935 is 1.1.

Table 3. Properties of the diffuse emission in regions A–D. Column 1 is the region name, column 2 is the integrated flux density at 610 MHz, column 3 is the *k*-corrected integrated flux density as 610 MHz, column 4 is the surface brightness and column 5 is the *k*-corrected power at 610 MHz.

Region	$S_{610\rm MHz}$ (mJy)	$S_{610\rm MHz,k\text{-}corr}$ (mJy)	$I_{610\rm MHz}$ (μJy arcsec^{-2})	$P_{610\rm MHz}$ (10^{24} W Hz^{-1})
A	10.0 ± 2.0	12.0 ± 2.0	6.0 ± 1.0	9.0 ± 2.0
B	19.0 ± 3.0	–	11.0 ± 2.0	–
C	11.0 ± 2.0	–	6.3 ± 0.9	–
D	5.2 ± 0.8	4.7 ± 0.7	3.0 ± 0.4	3.4 ± 0.5

Notes. *k*-corrected flux and $P_{601\rm MHz}$ are calculated assuming a spectral index of 0.7 for region D and 1.4 for region A.

Table 4. Sources within GMRT primary beam half-power point. Column 1–4 list the RA and Dec. values of each source as well as error in the positions. Column 5 lists the integrated flux density at 610 MHz, column 6 is the integrated flux density measured from NVSS, column 7 is the offset between the source position measured in GMRT and NVSS. Column 8 is the spectral index of the source.

RA (h:m:s)	RA err. (s)	Dec. (d:m:s)	Dec. err. (arcsec)	$S_{610,\,\mathrm{GMRT}}$ (mJy)	S_{NVSS} (mJy)	Offset (arcsec)	α
22:44:31.20	0.10	−09:41:07.80	2.80	2.18 ± 0.32	–	–	–
22:44:26.90	0.00	−09:26:36.40	0.30	33.91 ± 0.73	48.16 ± 1.22	3.1	−0.42 ± 0.09
22:44:29.60	0.10	−09:45:39.50	1.30	6.22 ± 0.44	6.37 ± 0.75	1.3	−0.03 ± 0.38
22:44:12.80	0.00	−09:34:22.60	0.50	13.09 ± 0.48	18.34 ± 0.99	1.4	−0.41 ± 0.18
22:44:12.60	0.10	−09:46:29.40	2.30	2.50 ± 0.34	4.63 ± 0.73	5.6	−0.74 ± 0.58
22:44:02.40	0.00	−09:51:18.40	0.10	165.66 ± 0.67	143.02 ± 1.32	19.2	0.18 ± 0.03
22:44:03.20	0.10	−09:28:32.70	0.90	9.96 ± 0.51	7.56 ± 0.82	6.0	0.33 ± 0.33
22:43:56.60	0.10	−09:25:26.00	1.60	3.79 ± 0.37	–	–	–
22:43:49.40	0.00	−09:54:06.20	0.20	103.19 ± 0.61	87.99 ± 1.16	1.5	0.19 ± 0.04
22:43:40.30	0.10	−09:42:31.70	1.40	6.06 ± 0.44	–	–	–
22:43:39.10	0.10	−09:34:42.30	1.50	10.41 ± 0.49	–	–	–
22:43:38.40	0.20	−09:44:28.40	3.30	2.85 ± 0.37	–	–	–
22:43:35.60	0.10	−09:30:42.60	2.40	2.92 ± 0.36	–	–	–
22:43:34.40	0.10	−09:33:41.30	2.90	3.69 ± 0.35	–	–	–
22:43:28.60	0.10	−09:28:00.50	1.30	7.62 ± 0.44	–	–	–
22:43:27.80	0.10	−09:47:10.00	2.50	1.91 ± 0.29	–	–	–
22:43:25.80	0.00	−09:39:11.40	0.50	16.16 ± 0.48	6.91 ± 0.90	3.2	1.02 ± 0.37
22:43:24.90	0.00	−09:33:49.50	0.90	20.67 ± 1.03	6.45 ± 0.77	2.3	1.40 ± 0.36
22:43:23.70	0.10	−09:50:52.60	2.80	3.10 ± 0.36	–	–	–
22:43:18.80	0.00	−09:18:54.40	0.30	22.85 ± 0.50	18.54 ± 0.99	1.5	0.25 ± 0.16
22:43:18.60	0.10	−09:44:52.20	1.00	8.76 ± 0.47	4.40 ± 0.63	2.2	0.83 ± 0.42
22:43:09.20	0.10	−09:36:09.60	1.20	21.34 ± 0.85	–	–	–
22:43:00.00	00.20	−09:34:56.20	3.90	2.89 ± 0.36	–	–	–
22:42:53.50	0.10	−09:22:49.10	2.30	3.33 ± 0.35	–	–	–
22:42:16.30	0.10	−09:31:53.10	2.40	2.49 ± 0.35	–	–	–

3.2.1 *Field sources*

In order to further examine the flux scale, the GMRT data were imaged with full uvrange, a Briggs weighting robust parameter of 0 and tapered close to the NVSS resolution. The software PYBDSM[3] was used to detect sources in both the NVSS and the GMRT maps. PYBDSM works by detecting all pixels in the map above a set peak threshold. It will then form islands of contiguous emission down to a set island threshold around the identified peak pixels. Gaussians are then fit to the islands and the Gaussians are grouped into individual sources. The flux densities of the sources are calculated by summing the flux densities of the Gaussians and the error in the flux density is calculated by summing the uncertainties in the Gaussians in quadrature. For both the GMRT and the NVSS images, the peak threshold was set to 7σ and the island threshold was set to 5σ. Table 4 lists the detected sources and their flux densities in the GMRT and the NVSS maps. Table 4 also shows the calculated spectral index of each source that is detected in both maps. Fig. 6 shows the spectral indices for sources in the field versus their flux densities. The average spectral index is 0.2 ± 0.6. An average spectral index of $\alpha = 0.7$ is expected for most optically thin extragalactic radio sources due to the energy distribution of cosmic rays produced in shocks. However at low frequencies, the spectral index distribution of faint sources is expected to have a flat tail due to the flattening of blazar spectra at frequencies below 1 GHz. (Massaro et al. 2014).

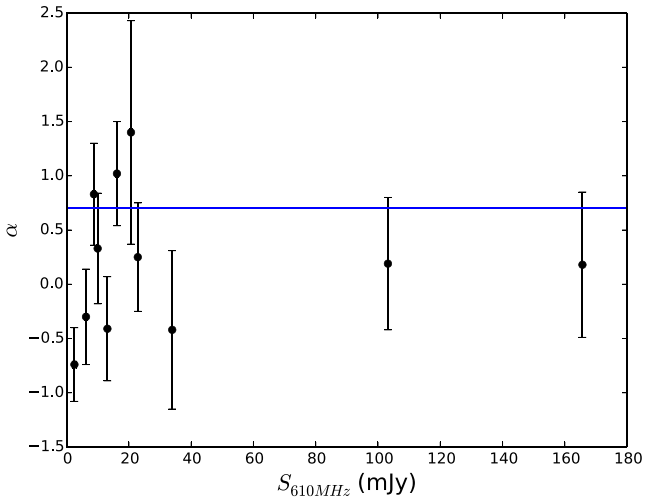

Figure 6. Spectral index of sources versus their flux density within the primary beam half power point. The blue line marks a spectral index of 0.7.

3.2.2 *Optical counterparts in regions A–D*

Fig. 7 shows the robust 0 images of regions A–D as well as the optical Sloan Digital Sky Survey (SDSS) images of each region. The locations of discrete radio sources are marked. Galaxies within the redshift slice $z \pm 0.04(1 + z)$ are deemed to be associated with the cluster (Wen, Han & Liu 2009). Table 5 lists the radio sources found in each region and their optical counterparts. An optical source was deemed to be the radio source's counterpart if the optical source was within one full width at half-maximum (FWHM) of the GMRT beam from the radio source. If more than one optical source lies with a FWHM of the radio source, then the source closest to the centroid of the radio source is deemed to be the optical counterpart.

[3] PYBDSM documentation: http://www.astron.nl/citt/pybdsm/

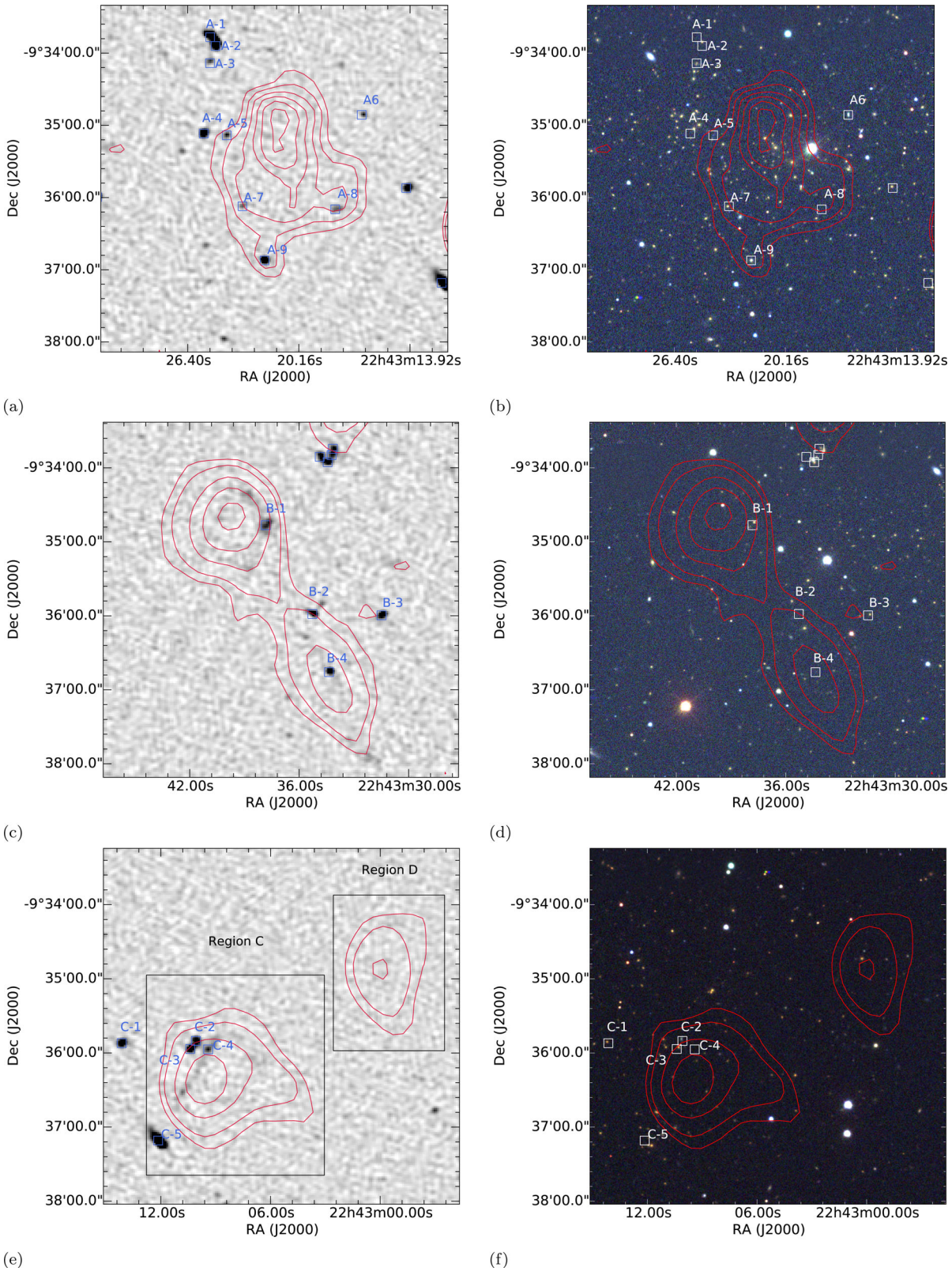

Figure 7. Grey-scale images show the robust 0 high-resolution GMRT data in the left-hand column and the red giant branch image of SDSS D12 *i*, *r* and *g* filters in the right-hand column. The high-resolution GMRT data has an rms noise of 40 μJy beam^{-1} and a resolution of 4.84 arcsec × 4.15 arcsec. The uvtapered GMRT images are overlaid in each image. The resolution of the uvtapered GMRT image is 44.89 arcsec × 33.70 arcsec. Radio point sources have been subtracted from the uvtapered image using models extracted from the high-resolution GMRT image shown in the grey scale. The locations of discrete radio sources detected by PYBDSM are marked by blue boxes in the left-hand column and by white boxes in the right-hand column. The first row shows images for region A with contours are at $-3, 3, 4, 5, 6, 7, 8, 9, 10, 15, 20 \times \sigma_{\rm rms}$ where $\sigma_{\rm rms} = 200$ μJy beam^{-1}. The middle row shows images for region B and the last row shows images for regions C and D with contours at $-3, 3, 5, 10, 15, 20 \times \sigma_{\rm rms}$ where $\sigma_{\rm rms} = 200$ μJy beam^{-1}.

Table 5. Sources within different regions. Column 1 is the region name and column 2 is the source name. Column 3 and 4 are the position of the sources in RA and Dec. Column 5 is the integrated flux density at 610 MHz, column 6 is the name of the SDSS optical counterpart, column 7 is the offset between the position of the GMRT source and the SDSS counterpart. Column 8 is the sources position relative to the cluster.

Region	Source	RA (h:m:s)	Dec. (d:m:s)	S_{610} (mJy)	SDSS source	Offset (arcsec)	Position
Region A	A-1	22:43:25.1	−09:33:46.8	3.62 ± 0.07	SDSS J224324.84-093350.9	3.05	Cluster member
	A-2	22:43:24.8	−09:33:54.0	5.18 ± 0.07	SDSS J224324.84-093350.9	3.05	Cluster member
	A-3	22:43:25.1	−09:34:08.5	0.61 ± 0.07	SDSS J224325.14-093408.7	0.25	Cluster member
	A-4	22:43:25.5	−09:35:06.8	1.94 ± 0.07	SDSS J224325.30-093503.1	4.68	Cluster member
	A-5	22:43:24.2	−09:35:08.3	0.52 ± 0.08	–	–	–
	A-6	22:43:16.6	−09:34:51.3	0.48 ± 0.08	SDSS J224316.63-093451.4	0.17	Foreground source
	A-7	22:43:23.3	−09:36:07.2	0.37 ± 0.08	SDSS J224323.40-093607.5	1.17	Cluster member
	A-8	22:43:18.1	−09:36:09.8	0.84 ± 0.06	–	–	–
	A-9	22:43:22.1	−09:36:52.2	2.02 ± 0.08	SDSS J224322.08-093652.4	0.18	Foreground source
Region B	B-1	22:43:37.8	−09:34:46.6	2.73 ± 0.05	SDSS J224337.71-093444.5	2.76	Cluster member
	B-2	22:43:35.3	−09:35:58.7	1.47 ± 0.07	–	–	–
	B-3	22:43:31.5	−09:35:59.7	1.46 ± 0.07	SDSS J224331.40-093558.9	1.47	Cluster member
	B-4	22:43:34.4	−09:36:45.6	1.24 ± 0.08	–	–	–
Region C	C-1	22:43:14.1	−09:35:52.1	1.71 ± 0.07	SDSS J224314.19-093551.1	1.12	Cluster member
	C-2	22:43:10.1	−09:35:50.3	1.56 ± 0.07	SDSS J224310.12-093548.7	1.74	Foreground source
	C-3	22:43:10.4	−09:35:56.8	1.50 ± 0.07	SDSS J224310.28-093555.4	2.09	Cluster member
	C-4	22:43:09.4	−09:35:57.1	1.31 ± 0.06	–	–	–
	C-5	22:43:12.1	−09:37:10.8	6.83 ± 0.08	SDSS J224311.92-093714.8	5.15	Cluster member

3.2.3 *Region A*

Region A is detected in the tapered image shown in Fig. 4 at a 5σ level. It is not detected at a significant level in either the untapered image, shown in Fig. 3, or the high-resolution image used to subtract the point sources. The emission at the 3σ level fills roughly the same region as the X-ray emission, shown in Fig. 4. The radio emission appears to be extended along an axis almost perpendicular to the extension of the X-ray emission. In Fig. 7(a), there are no compact radio sources coincident with or near the peak of region A and so the diffuse emission is unlikely to be associated with a single discrete source. At a redshift 0.447, region A has a LLS of approximately 0.92 Mpc.

3.2.4 *Region B*

To the east of the cluster, complex diffuse emission can be seen in both the tapered and untapered image. The emission has an LLS of approximately 1.7 Mpc. In Fig. 7(c), there are two peaks in the emission. The southern peak is coincident with a discrete radio source, B-4, at J22:43:34.4 -09:35:58.6. There is no SDSS, X-ray or infra-red counterpart for this source. It is possible that the optical source has a high redshift that puts it outside the range of SDSS. This would place the source behind the cluster. The northern peak is centred near source B-1 at J22:43:37.8 -9:34:46, which is located within the cluster. In Fig. 8, the northern peak is resolved into an arc of emission with one end of the arc coincident with B-1. In the untapered image, there is no emission detected connecting the northern and southern areas of region B.

3.2.5 *Regions C and D*

To the west of the cluster, there is a second region of complex diffuse emission. Again this can be seen in both the tapered and untapered maps. There appear to be two separate sources. The first, region C, is brighter and appears to coincident with at least two discrete sources, C-2 and C-3. A narrow linear structure is evident in the highest resolution grey-scale image as well as the untapered image of region C in Fig. 9. The linear structure extends from the north-west to south-east. Region C has an LLS of approximately 0.76 Mpc

The second region, region D, is on the edge of the cluster's virial radius. There are no discrete radio or optical sources evident in the region. It has an LLS of approximately 0.68 Mpc. The eastern side of region D is curved while the western side of region D is somewhat flatter.

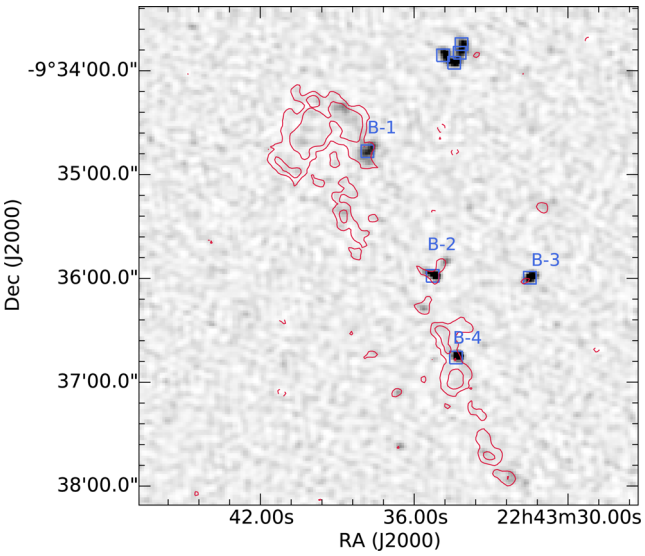

Figure 8. Grey-scale images show the robust 0 high-resolution GMRT data for region B. Red contours show naturally weighted image. Contours are at -3, 3, 5, 10, 15, 20 × $\sigma_{\rm rms}$ where $\sigma_{\rm rms}$ = 45 μJy beam^{-1}. The resolution of the GMRT image is 7.44 arcsec × 6.06 arcsec. Radio point sources have been subtracted from the naturally weighted image using models extracted from the high-resolution GMRT image shown in the grey scale. The blue squares mark discrete radio sources.

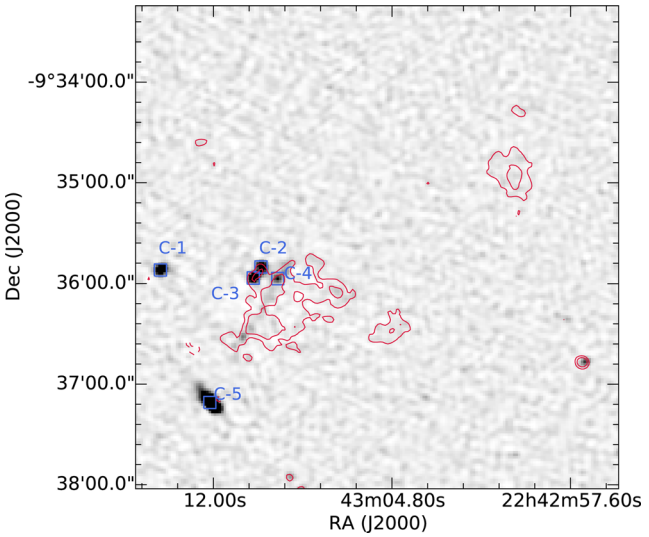

Figure 9. Grey-scale images show the robust 0 high-resolution GMRT data for regions C and D. Red contours show naturally weighted image. Contours are at -3, 3, 5, 10, 15, 20 $\times\ \sigma_{\rm rms}$ where $\sigma_{\rm rms} = 45\ \mu$Jy beam^{-1}. The resolution of the GMRT image is 7.44 arcsec $\times$ 6.06 arcsec. Radio point sources have been subtracted from the naturally weighted image using models extracted from the high-resolution GMRT image shown in the grey scale. The blue squares mark discrete radio sources.

4 DISCUSSION

4.1 A giant radio halo in MACS J2243.3-0935

Fig. 4 shows the X-ray emission of the cluster with the radio contours of region A overlaid. The morphology, size and position of region A are consistent with that of a giant halo.

4.1.1 *Spectral index*

As discussed in Section 3.2.3, Region A is clearly detected in the GMRT 610 MHz image, however it is not detected in the NVSS image and in the KAT-7 image all cluster emission is unresolved. Without high-resolution data at 1.822 GHz, it is not possible to disentangle emission in region A from emission in region B, C or D in the KAT-7 image. The NVSS image does not have the resolution or the sensitivity to subtract the discrete sources from the KAT-7 image. As such, we are only able to put a lower limit on the spectral index of the radio halo using the NVSS image. The rms noise of NVSS is 0.45 mJy beam^{-1}. Thus a 3σ upper limit flux density for the radio halo at 1400 MHz is 1.35 mJy beam^{-1}. Assuming the halo has the same spatial extent at 1400 MHz this gives an integrated upper limit on integrated flux of 8.2 mJy. Taken with the 610 MHz flux density of 10.0 $\pm$ 2.0 mJy, this gives a lower limit on the spectral index of $\alpha \geq 0.28$. Radio haloes are expected to have much steeper spectral indices than 0.28, however, NVSS does not have the surface brightness sensitivity to more tightly constrain the spectral index of region A.

Feretti et al. (2012) suggest a link between the average temperature of a cluster and the spectral index of radio haloes. They find that radio haloes in clusters with an average temperature between 8 and 10 keV have an average spectral index of $\alpha = 1.4 \pm 0.4$. MACS J2243.3-0935 has an temperature of 8.24 $\pm$ 0.92 K and so an estimate spectral index of $\alpha = 1.4$ will be used in this paper to estimate the properties of the halo in MACS J2243.3.

4.1.2 *Scaling relations*

Using the spectral index stated above, the k-corrected radio power of the halo at 610 MHz is $(9.0 \pm 2.0) \times 10^{24}$ W Hz^{-1}. Fig. 10 shows the halo's position on the $P_{610\,\rm MHz}-L_{\rm x}$ and $P_{610\,\rm MHz}-M_{500}$ diagrams. Fig. 10 is a reproduction of fig. 2 in Yuan et al. (2015) with the data point for MACS J2243.3-0935 included. Region A in MACS J2243.3-0935 is in good agreement with the power expected from the correlations show in Fig. 10, providing furthermore evidence that region A is a radio halo.

4.1.3 *Equipartition B-fields*

Beck & Krause (2005) provide a revised formula for the classical equipartition magnetic field,

$$B = \left\{ \frac{4\pi\,(2\alpha+1)\,(K_0+1)\,I_\nu E_p^{1-2\alpha} \left(\frac{\nu}{2c_1}\right)^{\alpha}}{(2\alpha-1)\,c_2 l c_4} \right\}^{\frac{1}{\alpha+3}}, \qquad (2)$$

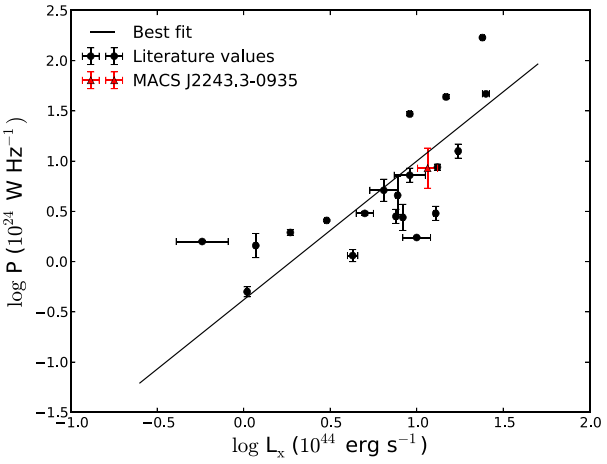

(a)

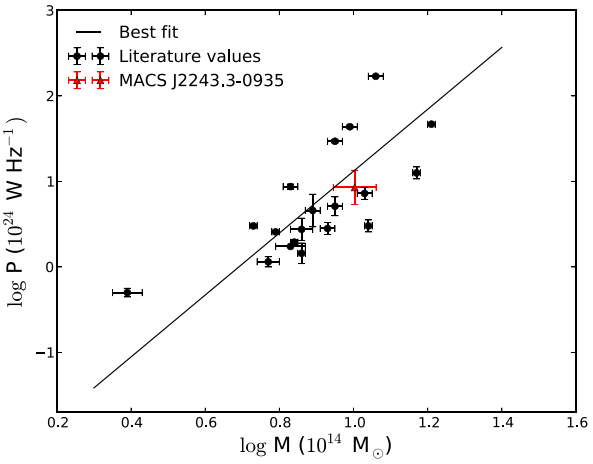

(b)

Figure 10. These plots marks the position of the halo in MACS J2243.3-0925 in red on the 610 MHz scaling relations examined in Yuan et al. (2015); (a) shows the $P_{610\,\rm MHz}-L_{\rm x}$ correlation and (b) shows the $P_{610\,\rm MHz}-M$ relation. Black data points are taken from Yuan et al. (2015).

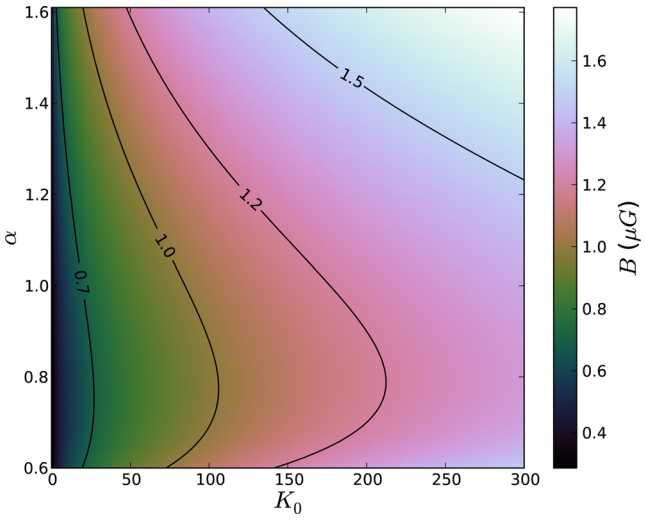

Figure 11. Equipartition magnetic field strength for region A for a range of values of α and K_0. Black contours mark regions of constant magnetic field strength.

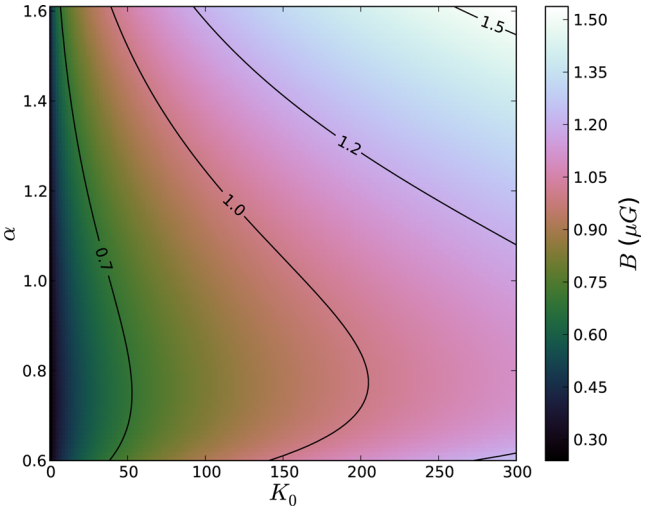

Figure 12. Equipartition magnetic field strength for region D for a range of values of α and K_0. Black contours mark regions of constant magnetic field strength.

where α is the spectral index, K_0 is the ratio of proton energy densities to electron energy densities, I_ν is the synchrotron intensity, E_p is the proton rest energy, ν is the observing frequency and l is the extent of the source along the line of sight. c_1 and c_3 are constants while c_2 is a function of the spectral index and c_4 is a function of the inclination of the source. See appendix A in Beck & Krause (2005) for definition of these variables.

There is much discussion in the literature on the precise value of K_0. Different CR injection mechanisms predict different values for K_0 for the ICM. For example, turbulent acceleration predicts $K_0 = 100$, production of secondary CRe predicts K_0 in the range of 100–300 and first order *Fermi* shock acceleration predicts values of K_0 in the range of 40–100 (Beck & Krause 2005). However, energy losses such as synchrotron and inverse Compton could inflate the value of K_0 to values much greater than 100. Vazza & Brüggen (2014) compare some of the current models for CR injection to radio and *Fermi* data on clusters. They find that values of $K_0 \geq 100$ require gamma emission above the derived *Fermi* upper limits, suggesting that $K_0 \leq 100$.

Using equation (2), we calculate the equipartition magnetic field of the cluster in region A and region B for different values of α and K_0. Fig. 11 shows the results for region A while Fig. 12 shows the results for region B. For both regions, magnetic field strengths vary from less than 0.5 μG for flat spectral indices and small values of K_0 to 1.5 μG for steep spectral indices and high values of K_0.

4.2 Possible radio relics in MACS J2243.3-0935

4.2.1 Region B

There are four possible explanations for the diffuse emission in Region B. The first is that it is merely a superposition of emission from sources at different redshifts. The second is that the emission is associated with the interaction of sources at the same redshift. The third is that the emission is from a giant radio galaxy (GRG). And finally the emission could be a radio relic.

The LLS of region B is consistent with both a GRG or a radio relic. The position of region B at the periphery of a cluster is expected for a radio relic while GRGs are more commonly found in less dense regions such as galaxy groups (Malarecki et al. 2015).

The double-peaked morphology of region B is unusual for a radio relic. A possible explanation for these localised regions of increased emission, in the context of a radio relic, is that these peaks coincide with areas of fossil active galactic nuclei activity. The fossil CRe in these areas would be accelerated to higher energies and lead to a localized increase in emission.

The northern peak in Fig. 8 could also be interpreted as a bow shock in the lobe of a GRG. However it seems more likely that this is instead emission associated with B-1 and that B-1 is a head-tail radio galaxy.

While the linear size of region B is consistent with a radio relic or GRG, comparison between Figs 3 and 4 suggest that region B is not a region of continuous emission, but instead a series of radio galaxies that are unresolved in the tapered image, thus ruling out a radio relic and GRG. This would place B-1 and B-4 as the sources of the northern and southern peaks, respectively.

B-4 and B-2 do not have optical counterparts in SDSS. They are likely background galaxies outside the redshift range of SDSS, suggesting that region B is a superposition of sources at different redshifts.

4.2.2 Region C

Fig. 9 shows the high-resolution GMRT data for region C with the naturally weighted contours overlaid. The morphology of region C seen in Fig. 9 is consistent with bent tail radio galaxy. Bent tail galaxies are commonly found in galaxy clusters where the dense ICM warps the radio jet (Mao et al. 2009; Pratley et al. 2013). Such sources have been used to probe different physical properties of the ICM, including the density (Freeland, Cardoso & Wilcots 2008) and magnetic field strength (Clarke, Kronberg & Böhringer 2001; Vogt & Enßlin 2003; Pratley et al. 2013). However, due the cluster of discrete radio sources, C-2, C-3 and C-4, a superposition of sources cannot be ruled as an explanation for the emission in region C.

The position of region C in the cluster and its LLS are also consistent with that of a radio relic. There is evidence to suggest that some radio relics are generated when shocks re-accelerated fossil plasma from radio galaxies (Enßlin & Gopal-Krishna 2001; Bonafede et al. 2014; Shimwell et al. 2015). In such a scenario, region B could be a produced when fossil emission from C-2, C-3

or C-4 was re-accelerated by a merger shock. However, without knowing how the spectral index varies across the source, it is not possible to differentiate between a radio relic and a bent tail radio galaxy.

4.2.3 Region D

NVSS and FIRST do not detect any radio sources in Region D. The rms noise of NVSS is 0.45 mJy beam^{-1}. Thus, a 3σ upper limit flux density for region D at 1400 MHz is 1.35 mJy beam^{-1}. Assuming region D has the same spatial extent at 1400 MHz this gives an upper limit on the integrated flux density of 2.0 mJy. Taken with the 610 MHz flux density of 5.2 mJy, this gives a lower limit on the spectral index of $\alpha \geq 0.7$.

The grey-scale image in Fig. 9 shows data from baselines longer than 4 kλ imaged with a Briggs robust parameter of 0 for both region C and region D with the contours for the naturally weighted, point source subtracted image overlaid. No compact radio sources can be seen in this image coincident with or near the peak of region D and so the diffuse emission is unlikely to be associated with a single discrete source.

With an LLS of 0.68 Mpc, Region D is consistent with that of a radio relic. The lack of radio point sources in region D suggests this emission is not associated with a discrete source. Region D is about twice the length on the north–south axis as on the east–west axis, which is consistent with the morphology of elongated radio relics. Radio relics are likely formed by shocks produced by either major/minor cluster mergers or through the infall of the warm-hot intergalactic medium (WHIM) on to the cluster. Shocks produced by cluster mergers are expected to have a Mach number less than 5 (Skillman et al. 2008). Hong et al. (2014) study the properties of shocks at cluster outskirts and suggest that around half of radio relics with Mach numbers greater than 3, as well as relatively flat radio spectra, are infall shocks. To date, only a few relics have been described as infall relics in the literature. For example, Brown & Rudnick (2011) suggest that the radio relic 1253+275 in the Coma cluster is caused by the infalling group NGC 4839, while Pfrommer & Jones (2011) model the structure of the head tail radio galaxy NGC 1265 by assuming that the galaxy passed through an accretion shock on to the Perseus cluster. Pfrommer & Jones (2011) calculate the Mach number of the inferred accretion shock in the Perseus cluster to be approximately $\mathcal{M} = 4.2$.

MACS J2243.3-0935 is the central cluster in the supercluster SCL2243-0935. Fig. 13 shows the number density of SDSS galaxies in the region of MACS J2243-0935. The galaxy density at each point was calculated by counting the number of galaxies that fell in each pixel. The resultant map was then smoothed with a Gaussian of width 42 arcsec. Galaxies were chosen to be in the photometric redshift bin $0.39 < z < 0.5$ and within 4 Mpc of the cluster centre. This redshift bin was chosen to account for uncertainties in the photometric redshift error and a large spatial region was chosen to include the filamentary structure in the supercluster. Region D is located at the virial radius where one of the supercluster filaments, AH in Schirmer et al. (2011), meets MACS J2243.3-0935. The location of region D as well as the LLS are suggestive of an infall relic, however, multifrequency analysis would be required to properly determine the nature of the region.

In order to rule out Galactic foreground emission as an explanation for region D, Fig. 14 shows region D at multiple wavelengths. There is no significant emission in the Improved Reprocessing of the IRAS Survey (IRIS) (Miville-Deschenes & Lagache 2005), the Southern H-α Sky Survey Atlas (SHASSA) (Gaustad et al. 2001), the Wide-field Infrared Survey Explorer (WISE) (Wright et al. 2010) or *Planck*, and we conclude that region D is unlikely to be associated with Galactic foreground emission.

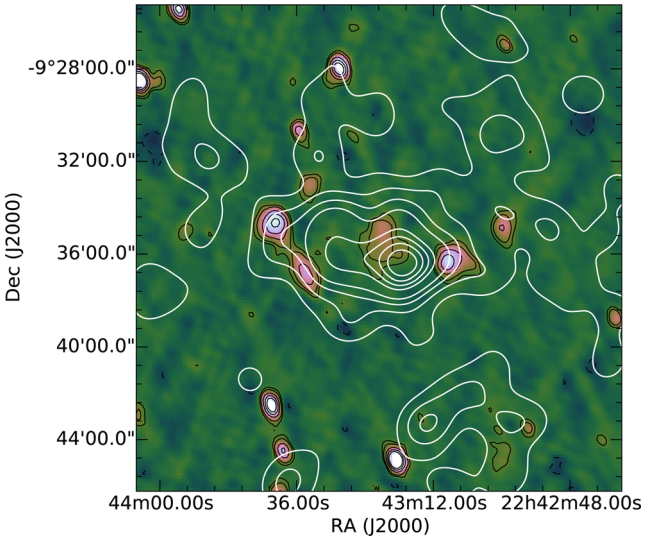

Figure 13. Colour-scale image of diffuse emission in MACS J2243.3-0935 with black contours overlaid showing the tapered image. Contours are at $-3, 3, 5, 10, 15, 20 \times \sigma_{\rm rms}$ where $\sigma_{\rm rms} = 200$ μJy beam^{-1}. Galaxy density contours overlaid in white. These contours are range from 20 per cent to 90 per cent of the peak value in steps of 10.

Given the coincidence of region D with a filament, the radio emission might alternatively be associated with the WHIM rather than a radio relic. There is no agreement on precise predictions for magnetic fields in filaments but estimates range from 10^{-4} to 0.1 μG (Dolag, Bartelmann & Lesch 1999; Brüggen et al. 2005; Ryu et al. 2008). In Section 4.1.3, the equipartition magnetic field estimates for region D for a spectral index of 0.7 are greater than the estimates for magnetic fields in the WHIM. Araya-Melo et al. (2012) model cosmic rays in large-scale structure and predict a flux density of 0.12 μJy beam^{-1} at a frequency of 150 MHz for a 10 arcsec^2 beam. This is much lower than the flux density measured in region D or in other possible radio detections of the WHIM (Bagchi et al. 2002; Farnsworth et al. 2013). The high flux density and magnetic field estimates for region D suggest that it is unlikely to be a radio detection of the WHIM.

5 CONCLUSION

We have discovered a radio halo in the merging cluster MACS J2243.3-0935 using GMRT observations at 610 MHz and KAT-7 observations at 1822 MHz. The radio halo has an integrated flux density of 10.0 ± 2.0 mJy, an estimated radio power at 1.4 GHz of $(3.2 \pm 0.6) \times 10^{24}$ W Hz^{-1} and an LLS of approximately 0.92 Mpc. We calculated the equipartition magnetic field in the region of the halo for a range of α and K_0 values and find that the equipartition magnetic field is of the order of 1 μG. Assuming a spectral index of $\alpha = 1.4$, the halo in MACS J2243.3-0935 lies on the empirical scaling relations observed for radio haloes.

We also detected a potential radio relic candidate to the west of the cluster. The candidate relic has an integrated flux density of 5.2 ± 0.8 mJy, an estimated radio power at 1.4 GHz of $(1.6 \pm 0.3) \times 10^{24}$ W Hz^{-1} and a LLS of 0.68 Mpc. The presence of a radio relic in MACS J2243.3-0935 would make this one of

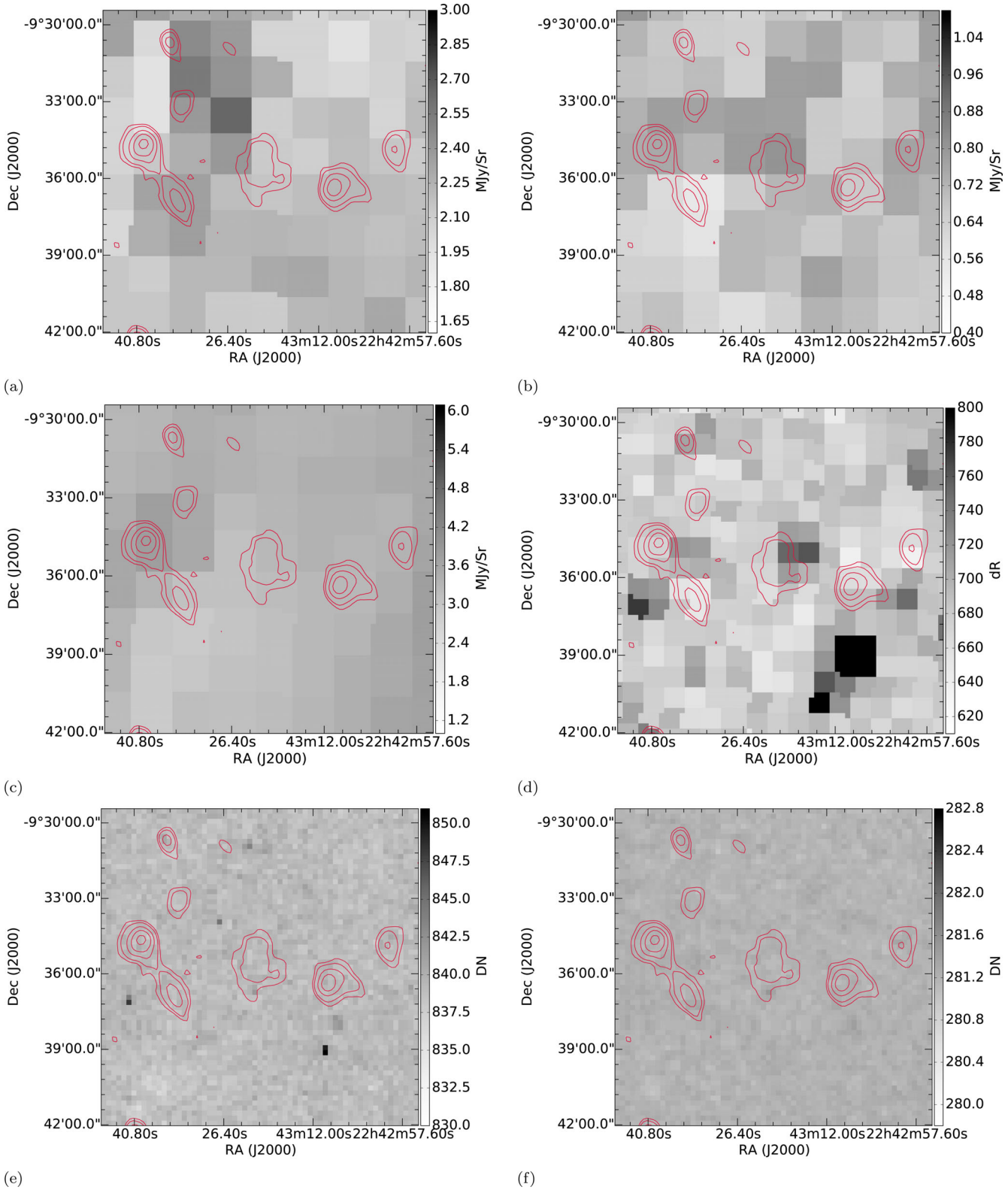

Figure 14. These images show MACS J2243.3-0935 at different wavelengths with red contours overlaid showing the tapered image. Contours are at 3, 5, 10, 15, 20 $\times\ \sigma_{\rm rms}$ where $\sigma_{\rm rms} = 200\ \mu{\rm Jy\,beam^{-1}}$. (a) IRIS 25 μm, (b) IRIS 60 μm, (c) IRIS 100 μm, (d) SHASS Hα, (e) *WISE* 12 μm, (f) WISE 22 μm.

only a handful of clusters that host both a halo and a relic. Due to the position of the relic candidate on the outskirts of the cluster, where a filament meets the cluster, we conclude that the candidate is consistent with an infall relic. We rule out the possibility of the emission being associated with the WHIM in a filament as the measured flux density and estimated equipartition magnetic field strength are both much larger than expected values for the WHIM. We also exclude foreground galactic emission as an explanation as there is no significant emission in IRIS, SHASSA Hα, *WISE* or *Planck*.

ACKNOWLEDGEMENTS

AMS gratefully acknowledges support from the European Research Council under grant ERC-2012-StG-307215 LODESTONE. The research of JLH and ZLW are supported by the National Natural Science Foundation of China (No. 11473034 and 11273029) and by the Strategic Priority Research Program 'The Emergence of Cosmological Structures' of the Chinese Academy of Sciences, Grant No. XDB09010200. We thank the staff of the GMRT who have made these observations possible. GMRT is run by the National Centre for Radio Astrophysics of the Tata Institute of Fundamental Research. We thank the staff of the Karoo Observatory for their invaluable assistance in the commissioning and operation of the KAT-7 telescope. The KAT-7 is supported by SKA South Africa and the National Science Foundation of South Africa. We thank the anonymous referee for their useful comments that improved the content of this paper.

REFERENCES

Araya-Melo P. A., Aragón-Calvo M. A., Brüggen M., Hoeft M., 2012, MNRAS, 423, 2325
Bagchi J., Enßlin T. A., Miniati F., Stalin C. S., Singh M., Raychaudhury S., Humeshkar N. B., 2002, New Astron., 7, 249
Basu K., 2012, MNRAS, 421, L112
Beck R., Krause M., 2005, Astron. Nachr., 326, 414
Becker R. H., White R. L., Helfand D. J., 1995, ApJ, 450, 559
Bock D. C.-J., Large M. I., Sadler E. M., 1999, AJ, 117, 1578
Bonafede A., Intema H. T., Brüggen M., Girardi M., Nonino M., Kantharia N., van Weeren R. J., Röttgering H. J. A., 2014, ApJ, 785, 1
Brown S., Rudnick L., 2011, MNRAS, 412, 2
Brüggen M., Ruszkowski M., Simionescu A., Hoeft M., Dalla Vecchia C., 2005, ApJ, 631, L21
Brunetti G., Jones T. W., 2014, Int. J. Mod. Phys. D, 23, 1430007
Brunetti G., Cassano R., Dolag K., Setti G., 2009, A&A, 507, 661
Cassano R. et al., 2013, ApJ, 777, 141
Chandra P., Ray A., Bhatnagar S., 2004, ApJ, 612, 974
Clarke T. E., Kronberg P. P., Böhringer H., 2001, ApJ, 547, L111
Colafrancesco S., 1999, in Boehringer H., Feretti L., Schuecker P., eds, Diffuse Thermal and Relativistic Plasma in Galaxy Clusters. Max-Planck-Institut für extraterrestrische Physik, Garching, p. 269
Condon J. J., Cotton W. D., Greisen E. W., Yin Q. F., Perley R. A., Taylor G. B., Broderick J. J., 1998, AJ, 115, 1693
De Gasperin F., Intema H. T., Williams W., Brüggen M., Murgia M., Beck R., Bonafede A., 2014, MNRAS, 440, 1542
Dolag K., Bartelmann M., Lesch H., 1999, A&A, 348, 351
Ebeling H., Edge A. C., Mantz A., Barrett E., Henry J. P., Ma C. J., van Speybroeck L., 2010, MNRAS, 407, 83
Enßlin T. A., Röttgering H., 2002, A&A, 396, 83
Enßlin T. A., Gopal-Krishna, 2001, A&A, 366, 26
Farnsworth D., Rudnick L., Brown S., Brunetti G., 2013, ApJ, 779, 189
Feretti L., 2002, in Pramesh Rao A., Swarup G., Gopal-Krishna eds, Proc. IAU Symp. 199, The Universe at Low Radio Frequencies. Kluwer, Dordrecht, p. 133
Feretti L., 2003, in Bowyer S., Hwang C.-Y., eds, ASP Conf. Ser. Vol. 301, Matter and Energy in Clusters of Galaxies. Astron. Soc. Pac., San Francisco, p. 143
Feretti L., Giovannini G., Govoni F., Murgia M., 2012, A&AR, 20, 54
Freeland E., Cardoso R. F., Wilcots E., 2008, ApJ, 685, 858
Gaustad J. E., McCullough P. R., Rosing W., Van Buren D., 2001, PASP, 113, 1326
Govoni F., Enßlin T. A., Feretti L., Giovannini G., 2001, A&A, 369, 441
Helmboldt J. F., Kassim N. E., Cohen A. S., Lane W. M., Lazio T. J., 2008, ApJS, 174, 313
Hong S. E., Ryu D., Kang H., Cen R., 2014, ApJ, 785, 133
Kravtsov A. V., Borgani S., 2012, ARA&A, 50, 353
Malarecki J. M., Jones D. H., Saripalli L., Staveley-Smith L., Subrahmanyan R., 2015, MNRAS, 449, 955
Mann A. W., Ebeling H., 2012, MNRAS, 420, 2120
Mantz A., Allen S. W., Ebeling H., Rapetti D., Drlica-Wagner A., 2010, MNRAS, 406, 1773
Mao M. Y., Johnston-Hollitt M., Stevens J. B., Wotherspoon S. J., 2009, MNRAS, 392, 1070
Massaro F., Giroletti M., D'Abrusco R., Masetti N., Paggi A., Cowperthwaite P. S., Tosti G., Funk S., 2014, ApJS, 213, 3
McMullin J. P., Waters B., Schiebel D., Young W., Golap K., 2007, in Shaw R. A., Hill F., Bell D. J., eds, ASP Conf. Ser. Vol. 376, Astronomical Data Analysis Software and Systems XVI. Astron. Soc. Pac., San Francisco, p. 127
Miville-Deschênes M.-A., Lagache G., 2005, ApJS, 157, 302
Offringa A. R., van de Gronde J. J., Roerdink J. B. T. M., 2012, A&A, 539
Pauliny-Toth I. I. K., Wade C. M., Heeschen D. S., 1966, ApJS, 13, 65
Perley R. A., Butler B. J., 2013, ApJS, 204, 19
Pfrommer C., Jones T. W., 2011, ApJ, 730, 22
Planck Collaboration XXIX, 2014, A&A, 571, A29
Planck Collaboration XXVII, 2015, A&A, preprint (arXiv:1502.01598)
Pratley L., Johnston-Hollitt M., Dehghan S., Sun M., 2013, MNRAS, 432, 243
Rengelink R. B., Tang Y., de Bruyn A. G., Miley G. K., Bremer M. N., Roettgering H. J. A., Bremer M. A. R., 1997, A&AS, 124, 259
Ryu D., Kang H., Cho J., Das S., 2008, Science, 320, 909
Schirmer M., Hildebrandt H., Kuijken K., Erben T., 2011, A&A, 532, A57
Shimwell T. W., Markevitch M., Brown S., Feretti L., Gaensler B. M., Johnston-Hollitt M., Lage C., Srinivasan R., 2015, MNRAS, 449, 1486
Skillman S. W., O'Shea B. W., Hallman E. J., Burns J. O., Norman M. L., 2008, ApJ, 689, 1063
Swarup G., Ananthakrishnan S., Kapahi V. K., Rao A. P., Subrahmanya C. R., Kulkarni V. K., 1991, Curr. Sci., 60, 95
Vazza F., Brüggen M., 2014, MNRAS, 437, 2291
Vogt C., Enßlin T. A., 2003, A&A, 412, 373
Voit G. M., 2005, Rev. Mod. Phys., 77, 207
Wen Z. L., Han J. L., 2013, MNRAS, 436, 275
Wen Z. L., Han J. L., Liu F. S., 2009, ApJS, 183, 197
Wright E. L., 2006, PASP, 118, 1711
Wright E. L. et al., 2010, AJ, 140, 1868
Yuan Z. S., Han J. L., Wen Z. L., 2015, ApJ, 813, 77

This paper has been typeset from a TEX/LATEX file prepared by the author.